Available online at www.sciencedirect.com
ScienceDirect
International Journal of Heat and Mass Transfer 51 (2008) 4573–4582
International Journal of HEAT and MASS TRANSFER
www.elsevier.com/locate/ijhmt

Technical Note

Introduction of a length correction factor for the calculation of laminar flow through microchannels with high surface roughness

José R. Valdés [a,*], Mario J. Miana [a], Miguel Martínez [a], Leticia Gracia [a], Thomas Pütz [b]

[a] *Instituto Tecnológico de Aragón, María de Luna 8, 50018 Zaragoza, Spain*
[b] *TRW Automotive, Carl Spaeter Strasse, 56070 Koblenz, Germany*

Received 5 December 2007; received in revised form 27 February 2008

Abstract

The main objective of this work is to introduce a length correction factor, based on CFD simulation results, in order to extend the method for taking into account the surface roughness effects in the calculation of laminar flow through rough microchannels described in [J.R. Valdés, M.J. Miana, T. Pütz, Numerical investigation of the influence of roughness on the laminar incompressible fluid flow through annular microchannels, Int. J. Heat Mass Transfer 50 (2007) 1865–1878], to surface roughness values much larger than the ones considered in the previous study. The method proposed in Valdés et al. (2007) consisted in building an equivalent smooth channel with the same flow resistance as the rough one. As in this case, the new method is validated with results of CFD simulations of microchannels with different roughness values.
© 2008 Elsevier Ltd. All rights reserved.

Keywords: Fluid flow; Microchannels; Surface roughness; Numerical simulation

1. Introduction

The aim of this work is to extend the calculation method described in [1] to microchannels with a wider range of relative roughness and peak density values, and to describe a procedure for developing such type of models. In [1], a method for taking into account the surface roughness effects in the calculation of the fluid flow through very narrow channels, with static walls and surface roughness was developed, based on 2D-axisymmetric CFD simulations. The relative roughness values were limited to 7%, while the linear peak density was limited to 180 peaks/mm (equivalent to a surface density of 32,400 peaks/mm^2, assuming an isotropic peak distribution). The aim of the present work is to extend said method to channel walls that might have much higher roughness and peak density, using CFD simulations of 3D channels formed by two parallel surfaces.

As in the previous work, the motivation for this work is the simulation of sealing systems, and in particular, the necessity to accurately calculate the flow rate that sometimes appears through the space that exists between a seal and the housing that contains it (see Fig. 1). Such case is sometimes found, among other applications, in the brake cylinder seals that separate the pressurized chamber and the chamber where the brake liquid is at atmospheric pressure.

Due to the very small width of the channels that are formed in these seal systems, the roughness of the surfaces involved plays a fundamental role. It is precisely in the domain formed by the rough surface of the metal and the elastic rubber material, which tries to adapt to the surface asperities, where a series of microchannels appear, in which it is important to analyse the fluid flow, in order to estimate possible leakages from the pressurized region.

The aim of this piece of work is to extend the methodology presented in [1], in order to widen the range of roughness values for which it is valid. The proposed methodology consists in running CFD simulations of the fluid

* Corresponding author. Tel.: +34 976 716211; fax: +34 976 716201.
E-mail address: jrvaldes@ita.es (J.R. Valdés).

0017-9310/$ - see front matter © 2008 Elsevier Ltd. All rights reserved.
doi:10.1016/j.ijheatmasstransfer.2008.03.001

Nomenclature

a,b,c	parameters of the fitting function
A	cross-sectional area
A_{eff}	average cross-sectional area
A_{wet}	channel surface in contact with the fluid
d	channel height
d_{h}	hydraulic diameter
h	average roughness peak height
$h_{\max}$	maximum peak height
K	flow resistance coefficient
L	length
P_{s}	static pressure
P_{t}	total pressure
Q	volume flow rate
Re	Reynolds number
v	flow velocity vector
V	mean flow velocity
V_{fluid}	net volume occupied by the fluid

Greek symbols

ε	relative roughness
Δ	increment
μ	fluid viscosity
ρ	fluid density
ρ_{peaks}	surface peak density
ξ	length correction factor

Subscripts

CFD	calculated from the CFD results
model	calculated with the model

flow in this type of channels, using its results to analyse in detail the fluid flow, and develop a model that allows its calculation from a reduced number of geometric and material parameters. This model can then be integrated in dynamic simulation models of the complete system, which allow to analyse and predict possible problems in the behaviour of the system, as well as to propose and analyse possible solutions and improvements.

In the previous work [1], the classical viscous flow theory was used, and it was established the coherence between the classical theory applied to flows through very narrow channels, and experimental and numerical results. In general terms, the recent articles on laminar flow through microchannels report a consistent behaviour between experiments, simulations and the classical theory [2–12]. The detailed experiments performed during the last years show that the laminar flows through microchannels are consistent with the classical theories and that the deviations that appeared in earlier papers are probably due to measurement uncertainties, errors in the diameter measurements, instrumentation errors, failure to consider other pressure losses present in the experiments, etc.

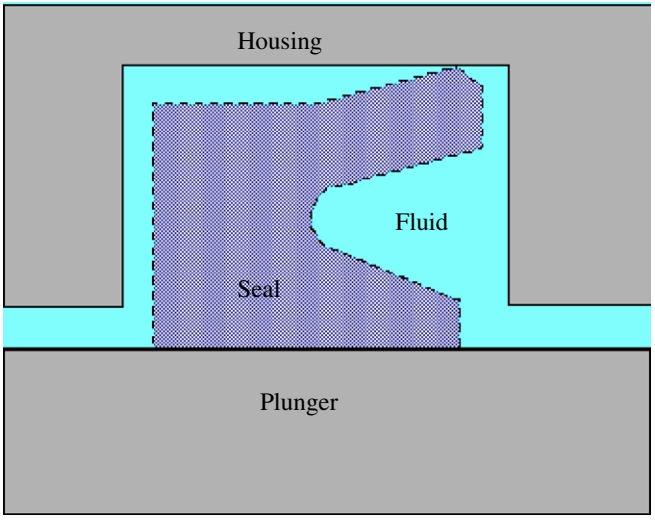

Fig. 1. Sketch of a typical seal system.

These results, combined with the numerical simulations of smooth channels presented in [1], and their comparison with the theoretical results, show that numerical simulations are a valid tool for simulating and analysing fluid flow in microchannels, and developing analytical models. CFD simulations allow to quickly run a large number of experiments, varying dimensions, roughness values, boundary conditions, etc, discarding many of the uncertainties associated to experimental tests on systems of such reduced dimensions.

Many articles report roughness effects as a cause for deviations from the macroscale theory [1,13,14,20,21], associating with them an increase in Poiseuille number with respect to conventional theory. Some authors [13,22] propose a roughness viscosity model to account for the effects of the surface roughness, which requires an experimentally determined coefficient. In general terms, the published articles show deviations of the classical theory due to the roughness, analyse and quantify these deviations, but do not propose analytical models.

No papers have been identified considering microchannel flow with relative roughness values larger than 10%. However, relative roughness values much larger than 10% can be found in the microchannels that appear in sealing systems, in which the rubber material, pressed against the asperities by the external pressure, tends to fill all the available space, thus making the relative roughness value tend to 100% and fulfilling the sealing functionality. However, before the pressure is high enough and the cavities are totally filled, there exist gaps through which the fluid can flow.

2. Laminar incompressible flow through rough microchannels

In general, for fully developed laminar flows in ducts of constant cross-section, there exists a linear relationship between the pressure drop and the volume flow rate [15]:

$$\Delta P_t = K \cdot Q \quad (1)$$

$$Q = A \cdot V \quad (2)$$

where ΔP_t is the total pressure difference between the channel inlet and the channel outlet, Q is the volume flow rate, A is the cross-sectional area and K is the flow resistance coefficient. ΔP_t refers to the pressure difference between the initial and final sections of the microtube, without considering the pressure losses upstream the tube inlet or downstream the tube outlet due to contractions or expansions. For flow between parallel surfaces, the flow resistance coefficient K is equal to [15]:

$$K = \frac{48 \cdot \mu \cdot L}{A \cdot d_h^2}, \quad (3)$$

where L is the length of the channel, μ is the fluid viscosity and d_h is the hydraulic diameter.

The method presented in [1] consists in building an equivalent smooth channel of the rough one, by defining the hydraulic diameter of the rough channel as

$$d_h = \frac{4V_f}{A_w}, \quad (4)$$

where V_f is the fluid volume and A_w is the wet area of the channel. An effective cross-sectional area can be defined for the channel as

$$A_{eff} = \frac{V_f}{L} \quad (5)$$

and the flow coefficient for a rough channel can be written as

$$K = \frac{48\mu L}{A_{eff} d_h^2} = \frac{4\mu A_w^2 L^2}{V_f^3}. \quad (6)$$

The accuracy of this expression for microchannels with relative roughness values up to 7% and peak density values up to 180 peaks/mm (32,400 peaks/mm^2) was checked in [1].

3. CFD simulation models and extended calculation method

Fig. 2 shows the general form of the channels that have been modelled. The channels are formed by two parallel plates of 100 μm of length and undetermined width (the lateral walls of the model are symmetry boundary conditions, being the width of the model 12 μm). The entrance and exit of the channel is slightly tapered, in order to resemble the typical progressive channelling of the flow due to the rounded corners of the seal.

Generally, the channels that appear between a seal and its housing are annular channels. A geometry formed by two narrow parallel surfaces, with symmetry boundary conditions at the lateral sides, represents one very small sector of the annular channel. In this type of channels, the dominating fluid direction is the axial direction, parallel to the walls, with small contributions in the radial and tangential directions due to the surface asperities. By modelling two parallel surfaces, including the surface asperities, the model captures the 3D flow, neglecting only the tangential flow at the lateral boundaries. The total flow for the whole annulus can be extrapolated from the results of one sector, as shown in Table 1 for a smooth channel. This table shows the computational flow resistance results for an annular channel of 10 mm of radius and 2.5 μm of height, and a plane channel of 2.5 μm of height and 12 μm of width, and the flow resistance of the annulus extrapolated from that of the plane channel. A complete model for the whole annular channel, including the surface roughness, would be excessively large.

Table 1 also shows that the CFD flow resistance coefficient differs from the analytical one, calculated with Eq. (6), in less than 1%, demonstrating the validity of the CFD code. Another validation was performed in [1], using 2D-axisymmetric channels.

On one of the surfaces pyramidal asperities of different sizes and densities have been modelled at random, producing five different models (see Fig. 3). For each the models, the upper wall is set at different heights with respect to the lower wall, in order to obtain different values of the channel height d and of the relative roughness ε, calculated as the ratio between the average peak height h and the channel hydraulic diameter, which equals $2d$ for parallel plate channels. In some cases, the upper wall has interference with the highest peaks. The values of the parameters of each model are listed in Table 2.

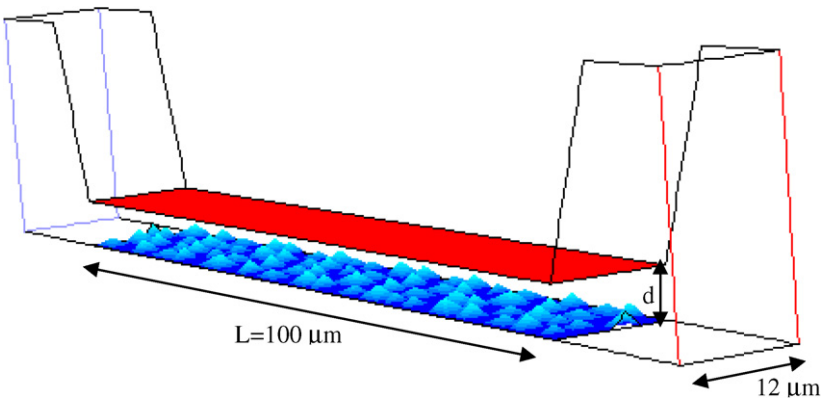

Fig. 2. Geometry of the microchannel models.

Table 1
Flow resistance results for annular and plane smooth channels

	Length (m)	Height (m)	Radius (m)	Width (m)	K_{theory} (Pa s/m^3)	K_{CFD} (Pa s/m^3)	$K_{extrapolated}$ (Pa s/m^3)
Annular channel	100E−6	2.5E−6	10E−3		1.64E+13	1.63E+13	1.62E+13
Plane channel	100E−6	2.5E−6	–	12E−6	8.58E+16	8.50E+16	–

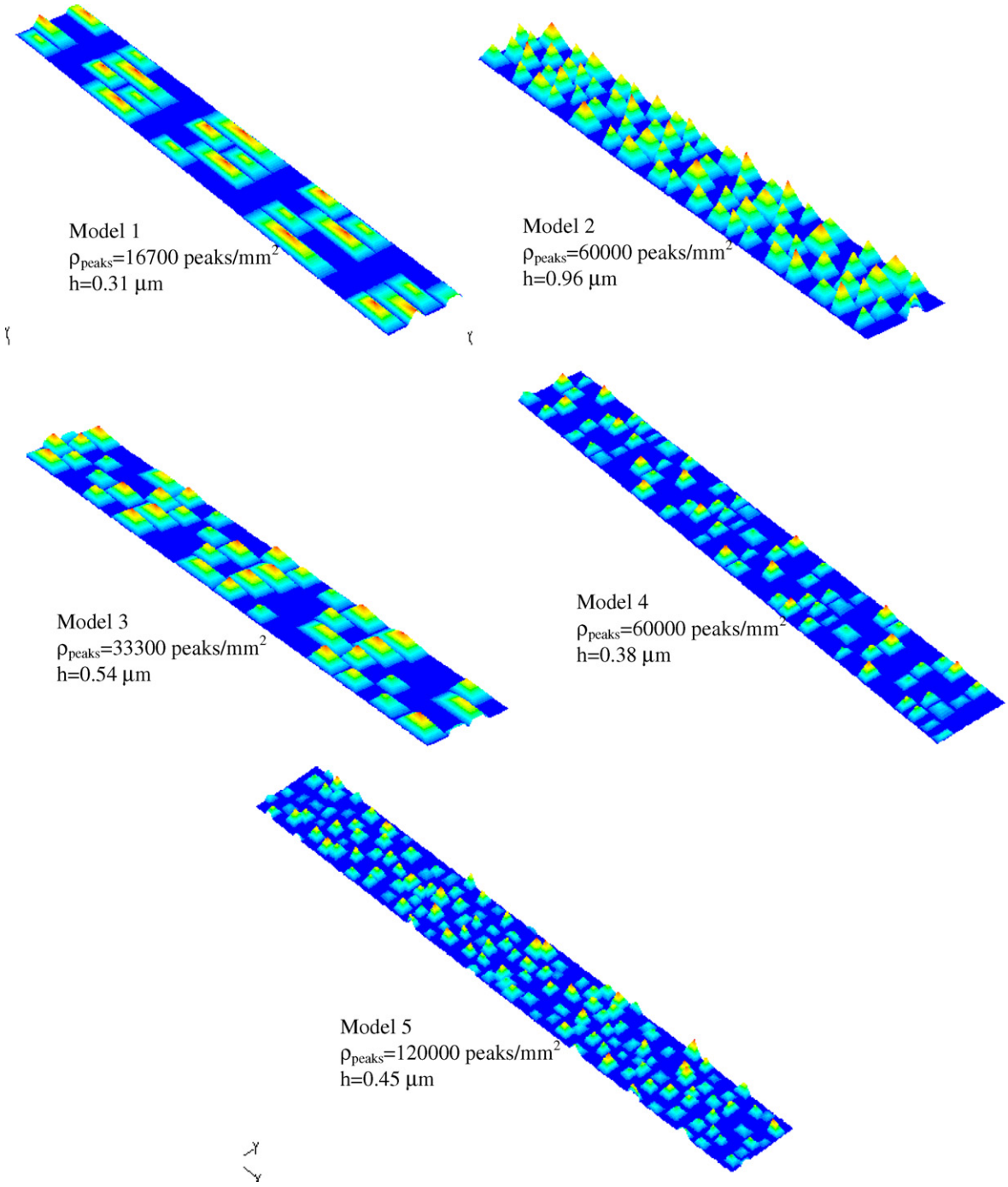

Fig. 3. Surface roughness models.

In all the models the inlet is defined as a pressure inlet at 10 bar and the pressure at the outlet is fixed at 0 bar. For some of the models, simulations have been also run imposing different inlet pressure values (1, 2, 5, 10 and 50 bar). The resulting pressure drop-volumetric flow rate relationship is totally linear (see Fig. 4); this means that the flow is only determined by the viscous (linear) losses and that the flow resistance coefficients K calculated from the

Table 2
Simulated models

	h_{max} (m)	h (m)	ρ_{peaks} (peaks/m^2)	d (m)	$\varepsilon = h/2d$ (%)
Model 1	1.50 E−6	0.31 E−6	1.67E+10	10.0E−06	1.55
				5.00E−06	3.10
				2.50E−06	6.20
				1.25E−06	12.40
				6.25E−07	24.80
Model 2	4.00 E−6	0.96 E−6	6.00E+10	5.00E−06	9.60
				2.50E−06	19.20
Model 3	2.50 E−6	0.54 E−6	3.33E+10	10.0E−06	2.70
				5.00E−06	5.40
				2.50E−06	10.80
				1.25E−06	21.60
Model 4	3.00 E−6	0.38 E−6	6.00E+10	10.0E−06	1.93
				5.00E−06	3.85
				2.50E−06	7.70
				1.25E−06	15.40
Model 5	3.00 E−6	0.45 E−6	1.20E+11	5.00E−06	4.53
				2.50E−06	9.05
				1.18E−06	19.18

CFD simulations at 10 bar, and which will be compared with the analytical ones, are valid for any other pressure value, as long as it is within the laminar flow regime. At the rest of the model boundaries a non-slip wall boundary condition is imposed, except for the lateral symmetry conditions.

Since our main motivation is the flow through very narrow channels in seal systems, and, in particular, in brake cylinder seals, a typical brake oil has been modelled (see properties in Table 3).

Assuming the hypotheses of laminar, incompressible and isothermal flow, steady-state regime, and Newtonian fluid, the resulting continuity (7) and momentum (8) equations are solved by means of the finite volume method, using the segregated implicit double precision solver of the commercial code FLUENT [16]. Double precision is required to capture accurately the small grid dimensions, areas and volumes. The momentum and continuity equations are solved sequentially. The continuity equation is used as an equation for pressure, but pressure does not appear explicitly in the continuity equation for incompressible

Table 3
Brake fluid properties at 23 °C (provided by TRW Automotive)

ρ	1057 kg/m^3
μ	0.0134 kg/m s

flows, since density is not directly related to pressure. The SIMPLE [17] (Semi-Implicit Method for Pressure-Linked Equations) algorithm is used for introducing pressure into the continuity equation. A detailed description of the numerical methods included in FLUENT can be found in Mathur and Murthy [18] or Kim et al. [19].

$$\vec{\nabla}\vec{v} = 0, \tag{7}$$

$$\mu\left(\frac{\partial^2 v_x}{\partial x^2} + \frac{\partial^2 v_x}{\partial y^2} + \frac{\partial^2 v_x}{\partial z^2}\right) = \frac{\partial P}{\partial x},$$
$$\mu\left(\frac{\partial^2 v_y}{\partial x^2} + \frac{\partial^2 v_y}{\partial y^2} + \frac{\partial^2 v_y}{\partial z^2}\right) = \frac{\partial P}{\partial y},$$
$$\mu\left(\frac{\partial^2 v_z}{\partial x^2} + \frac{\partial^2 v_z}{\partial y^2} + \frac{\partial^2 v_z}{\partial z^2}\right) = \frac{\partial P}{\partial z}. \tag{8}$$

For each model, a fine mesh of 1–1.5 million cells with a minimum of 10 cells across the channel is built (see Fig. 5). A refinement is applied, resulting in meshes of around 2 million cells, and yielding differences in mass flow rate, with respect to the original mesh, between 1.5% (model 1) and 3% (model 5). Finally, to check the mesh independency of these refined grids, an additional refinement is performed for one submodel (one height value) of each model, yielding meshes of around 2.5 million cells and differences in mass flow below 1% with respect to the results of the second meshes, which are the ones used for the analysis.

The indicator of calculation convergence is the scaled residual for each of the conserved variables [see 16], the mass flow imbalance throughout the domain and the mass flow stability along the calculation. In particular, the simulation is considered to be converged when each of the residuals is below 1e−12, the mass flow imbalance is four orders of magnitude smaller than the average mass flow rate value and the change in mass flow rate from one iteration to the

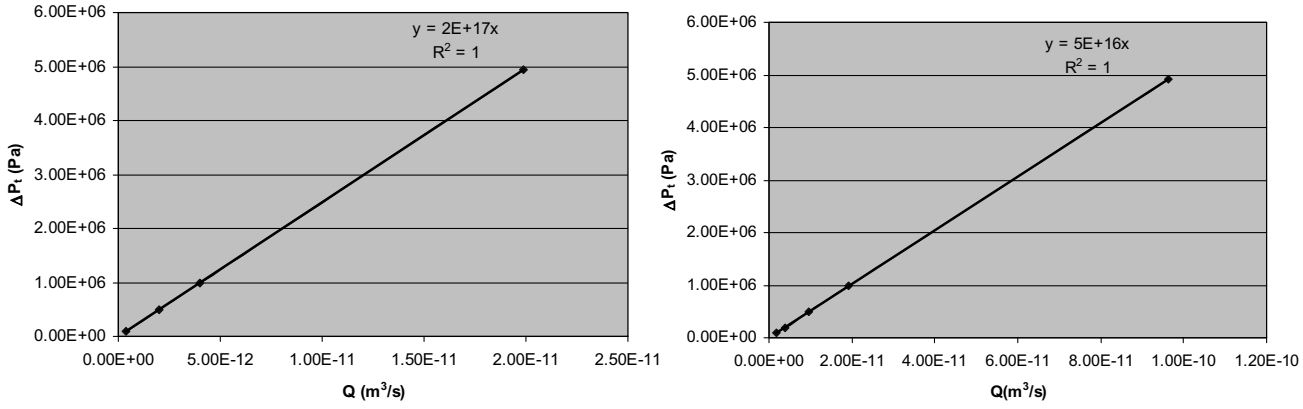

Fig. 4. Relationship ΔP_t vs. Q for two of the models: model 3, $d = 2.5$ μm (left); model 2, $d = 5$ μm (right).

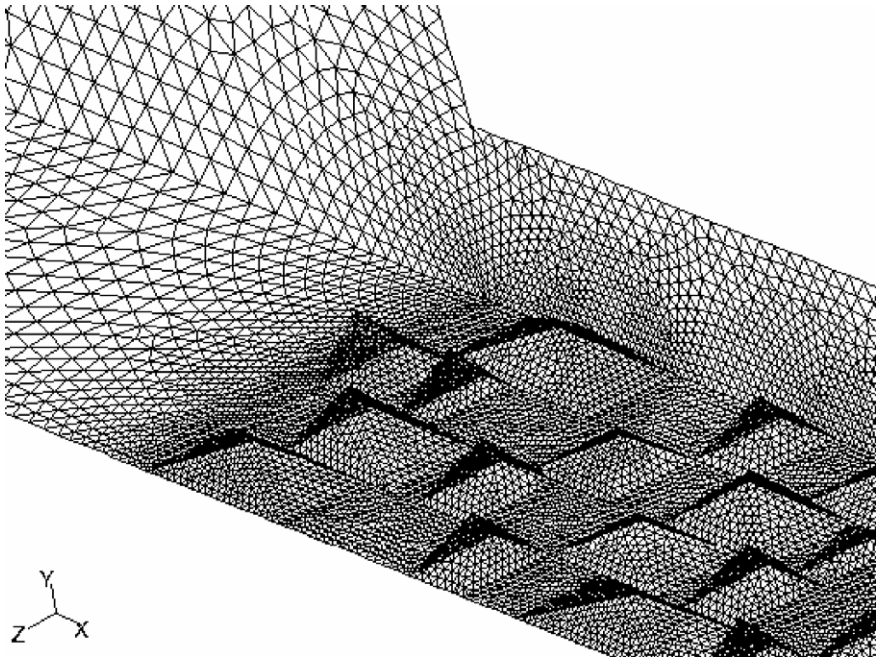

Fig. 5. Detail of the mesh of one of the models.

next is at least four orders of magnitude smaller than the average mass flow rate through the domain.

Table 4 summarizes the main features of the different models. Each submodel corresponds to a different position of the upper wall with respect to the lower wall, considering both cases in which the upper wall is not penetrated into the peaks and cases with penetration of the upper wall into the peaks. The values of the parameters needed to apply the calculation method are shown in the table. The average surface height, the fluid volume and the wet surface area are directly computed by the CFD solver (FLUENT) and the relative roughness, ε, is calculated as $h/2d$. The flow coefficient K is calculated using expression (6).

Using the CFD results of flow and total pressure drop, a "numerical" flow coefficient K_{CFD} can be calculated using expression (1), and then both results, K_{model} and K_{CFD}, are compared. Fig. 6 shows the deviation of K_{model} with respect to K_{CFD}, computed as the difference between K_{model} and K_{CFD} divided by K_{CFD} and written on a percentage basis.

The model yields deviations lower than 10% for low roughness and low peak density, but suffers a strong deviation as the relative roughness and peak density values increase. An extension of the model has to be proposed for high roughness and high peak density values. In Eq. (6), the travelled length L is considered as the length of the model (100 μm in this case), but, in reality, the fluid

Table 4
Main parameters of the different models and analytical flow resistance coefficient

	d (m)	ε (%)	V_f (m^3)	A_w (m^2)	d_h (m)	K (Pa s/m^3)
Model 1	10.0E−06	1.55	1.17E−14	2.54E−09	1.83E−05	1.65E+15
	5.00E−06	3.10	5.65E−15	2.54E−09	8.88E−06	1.44E+16
	2.50E−06	6.20	2.65E−15	2.54E−09	4.17E−06	1.40E+17
	1.25E−06	12.40	1.15E−15	2.51E−09	1.83E−06	1.66E+18
	6.25E−07	24.80	4.58E−16	2.07E−09	8.84E−07	1.80E+19
Model 2	5.00E−06	9.60	5.19E−15	3.49E−09	5.94E−06	3.52E+16
	2.50E−06	19.20	2.22E−15	3.23E−09	2.75E−06	3.83E+17
Model 3	10.0E−06	2.70	1.14E−14	2.78E−09	1.64E−05	2.08E+15
	5.00E−06	5.40	5.44E−15	2.78E−09	7.82E−06	1.94E+16
	2.50E−06	10.80	2.56E−15	2.78E−09	3.68E−06	1.86E+17
	1.25E−06	21.60	9.89E−16	2.43E−09	1.63E−06	2.44E+18
Model 4	10.0E−06	1.93	1.17E−14	2.82E−09	1.66E−05	1.99E+15
	5.00E−06	3.85	5.69E−15	2.82E−09	8.09E−06	1.73E+16
	2.50E−06	7.70	2.69E−15	2.81E−09	3.84E−06	1.62E+17
	1.25E−06	15.40	1.22E−15	2.60E−09	1.88E−06	1.48E+18
Model 5	5.00E−06	4.53	5.64E−15	3.02E−09	7.47E−06	2.04E+16
	2.50E−06	9.05	2.64E−15	3.01E−09	3.51E−06	1.97E+17
	1.18E−06	19.18	1.10E−15	2.71E−09	1.62E−06	2.25E+18

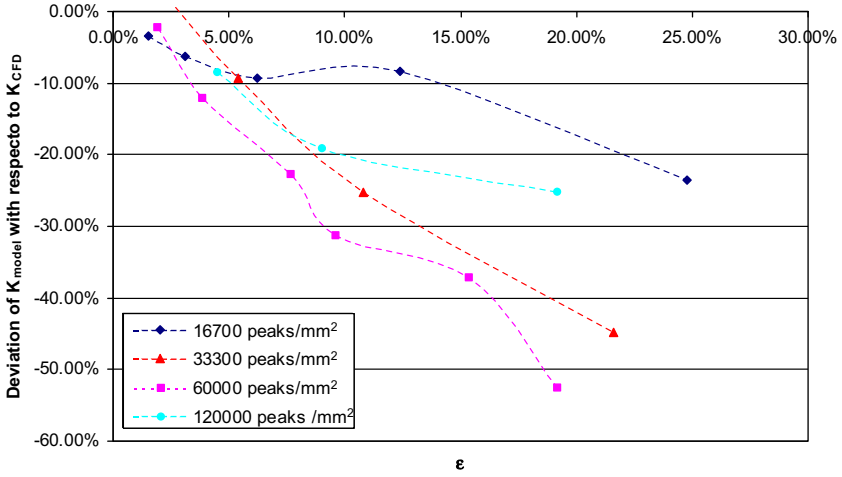

Fig. 6. Deviation of K_{model} with respect to K_{CFD}.

moving through the channel must travel a length which is longer than the actual model length. Moreover, this distance should increase as the peak density and the relative roughness increase. Therefore, a length correction factor ξ can be calculated from the CFD results using the following expression:

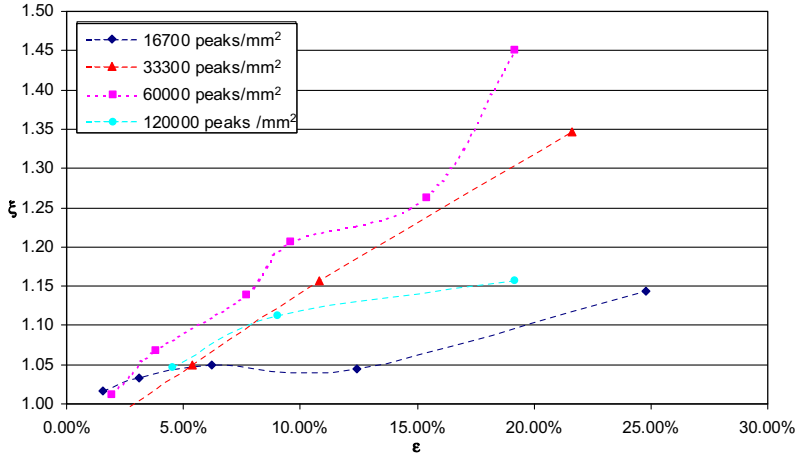

Fig. 7. Length correction factor ξ as a function of the relative roughness ε.

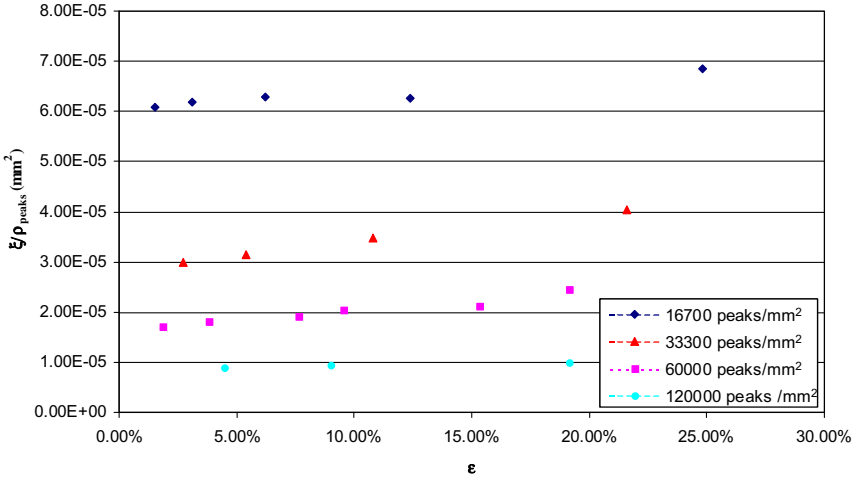

Fig. 8. Ratio ξ/ρ_{peaks} versus relative roughness.

$$K_{CFD} = \frac{4\mu A_w^2 (L \cdot \xi)^2}{V_f^3}. \quad (9)$$

The actual "effective" length travelled by the fluid is

$$L_{eff} = L \cdot \xi. \quad (10)$$

Fig. 7 shows the length correction factors calculated with Eq. (9) as a function of the relative roughness. The figure clearly shows how, for a given peak density, the length correction factor increases with roughness. However, it does not show an increasing trend with peak density, as the cases with 120,000 peaks/mm^2 fall between the 16,700 and the 33,000 peaks/mm^2 cases. A plot of the ratio ξ/ρ_{peaks} versus the relative roughness (Fig. 8) gives a much clearer view of the dependency of the length correction factor on both the peak density and the relative roughness. Fig. 8 shows that, for a given peak density, ξ/ρ_{peaks} increases in an approximately linear fashion with the relative roughness:

$$\frac{\xi}{\rho_{peaks}} = a \cdot \varepsilon + b. \quad (11)$$

For $\varepsilon = 0$ and $\rho_{peaks} = 0$, ξ tends to 1; therefore $b = 1/\rho_{peaks}$ and

$$\frac{\xi}{\rho_{peaks}} = a \cdot \varepsilon + \frac{1}{\rho_{peaks}}. \quad (12)$$

The computational values of ξ/ρ_{peaks} can be fitted to a function of this type, with a resulting value of $a = 3.18\text{E}{-5}$. The difference between the computational values and the ones obtained with Eq. (12) is below 5%, except in cases with high roughness and high peak density, where the value of ξ is overestimated. It is important to predict the value of ξ as well as possible, because the flow resistance coefficient depends on the square of the effective length. On the basis of the results of the previous fitting, we can try to include a crossed term of the type:

$$\frac{\xi}{\rho_{peaks}} = a \cdot \varepsilon + \frac{1}{\rho_{peaks}} - c \cdot \varepsilon \cdot \rho_{peaks}. \quad (13)$$

The fitting of this function to the computational CFD results yields $a = 4.6\text{E}{-5}$, $c = 2.8\text{E}{-10}$ (see Fig. 9), with a value of the coefficient of determination R^2 of 0.997.

Table 5
Geometric characteristics of the additional evaluation models

	d (m)	h (m)	ρ_{peaks} (peaks/m^2)	ε (%)
Model-6	10.0E−06	0.26E−06	6.00E+10	1.30
	5.00E−06	0.26E−06	6.00E+10	2.60
	2.50E−06	0.26E−06	6.00E+10	5.20
	1.25E−06	0.26E−06	6.00E+10	10.40
Model-7	10.0E−06	0.31E−06	6.00E+10	1.53
	5.00E−06	0.31E−06	6.00E+10	3.06
	2.50E−06	0.31E−06	6.00E+10	6.12
	1.20E−06	0.31E−06	6.00E+10	12.75
Model-8	5.00E−06	0.06E−06	2.50E+10	0.65
	2.50E−06	0.06E−06	2.50E+10	1.31
	1.25E−06	0.06E−06	2.50E+10	2.61
	6.25E−07	0.06E−06	2.50E+10	5.23
Model-9	10.0E−06	0.36E−06	9.00E+10	1.80
	5.00E−06	0.36E−06	9.00E+10	3.60
	2.50E−06	0.36E−06	9.00E+10	7.21
Model-10	3.00E−06	0.25E−06	5.00E+08	4.23
	1.05E−06	0.25E−06	5.00E+08	12.10

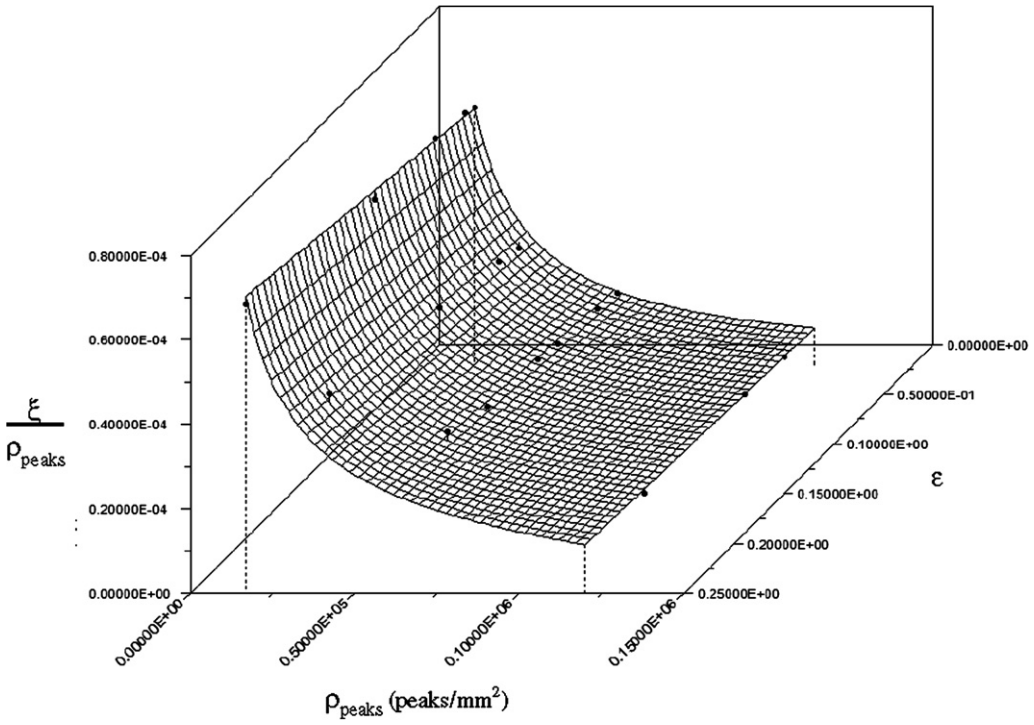

Fig. 9. Fitting of the correction factors.

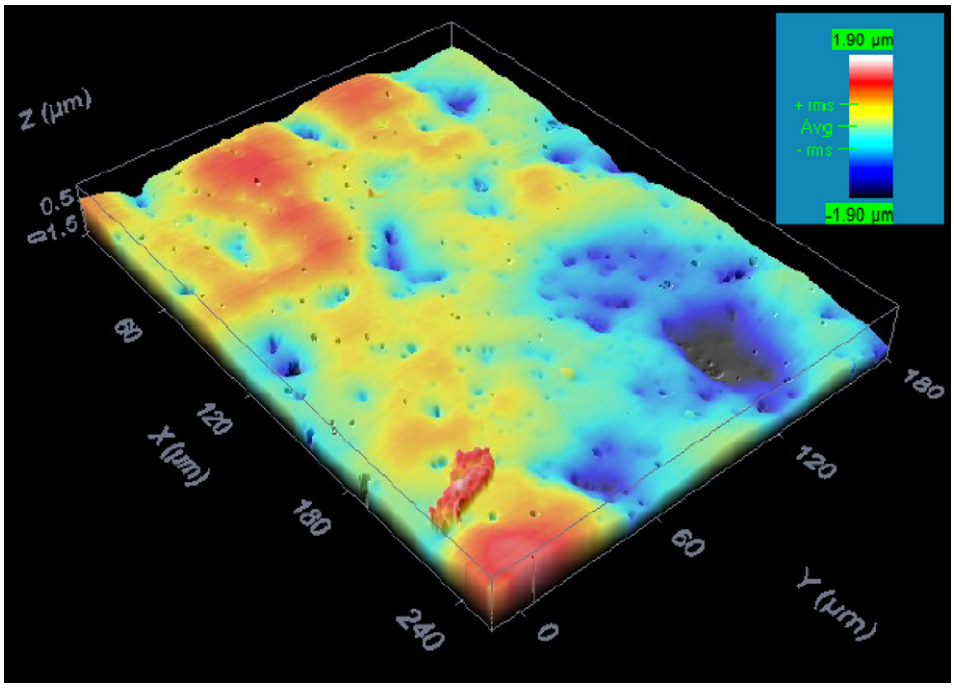

Fig. 10. Image of a plunger surface obtained by means of confocal microscopy techniques (RMS roughness = 0.63 µm, approximate peak density 400 peaks/mm^2).

Table 6
Final assessment of the proposed method

Model	ε (%)	ξ (CFD)	ξ	$\xi/\xi_{CFD} - 1$ (%)	K_{CFD} (Pa s/m^3)	K_{model} (Pa s/m^3)	$(K_{model}/K_{CFD}) - 1$ (%)
1	1.55	1.02	1.01	−0.6	1.70E+15	1.68E+15	−1.3
	3.10	1.03	1.02	−1.1	1.54E+16	1.51E+16	−2.3
	6.20	1.05	1.04	−0.6	1.54E+17	1.52E+17	−1.3
	12.40	1.04	1.09	3.9	1.78E+18	1.96E+18	7.9
	24.80	1.14	1.17	2.4	2.35E+19	2.47E+19	4.8
2	9.60	1.21	1.17	−3.2	5.12E+16	4.80E+16	−6.2
	19.20	1.45	1.34	−7.9	8.07E+17	6.84E+17	−15.2
3	2.70	1.00	1.03	3.6	2.07E+15	2.22E+15	7.4
	5.40	1.05	1.07	1.5	2.14E+16	2.20E+16	3.0
	10.80	1.16	1.13	−2.1	2.48E+17	2.38E+17	−4.1
	21.60	1.35	1.26	−6.1	4.43E+18	3.91E+18	−11.8
4	1.93	1.01	1.03	2.2	2.04E+15	2.13E+15	4.4
	3.85	1.07	1.07	0.1	1.97E+16	1.97E+16	0.1
	7.70	1.14	1.14	−0.2	2.09E+17	2.08E+17	−0.5
	15.40	1.26	1.27	−0.8	2.37E+18	2.39E+18	1.0
5	4.53	1.05	1.07	2.1	2.23E+16	2.33E+16	4.3
	9.05	1.11	1.13	2.0	2.44E+17	2.54E+17	4.0
	19.18	1.16	1.29	11.2	3.00E+18	3.71E+18	23.6
6	1.30	1.02	1.02	0.2	1.78E+15	1.79E+15	0.4
	2.60	1.05	1.05	−0.3	1.62E+16	1.61E+16	−0.6
	5.20	1.10	1.09	−0.8	1.65E+17	1.62E+17	−1.7
	10.40	1.15	1.18	2.6	1.95E+18	2.05E+18	5.2
7	1.53	1.03	1.03	−0.4	1.93E+15	1.91E+15	−0.9
	3.06	1.08	1.05	−2.0	1.78E+16	1.71E+16	−3.9
	6.12	1.13	1.11	−2.0	1.78E+17	1.71E+17	−4.0
	12.75	1.20	1.22	1.8	2.11E+18	2.19E+18	3.7
8	0.65	1.05	1.01	−4.2	1.29E+16	1.18E+16	−8.3
	1.31	1.05	1.01	−3.8	1.05E+17	9.76E+16	−7.4
	2.61	1.05	1.03	−2.6	8.78E+17	8.32E+17	−5.2
	5.23	1.04	1.05	0.6	7.02E+18	7.11E+18	1.2
9	1.80	1.07	1.03	−3.1	1.97E+16	1.85E+16	−6.1
	3.60	1.11	1.07	−3.6	1.94E+17	1.80E+17	−7.1
	7.21	1.12	1.14	1.5	1.75E+18	1.80E+18	3.0
10	4.23	1.05	1.00	−5.1	3.44E+16	3.10E+16	−9.9
	12.10	1.06	1.00	−5.0	1.21E+18	1.09E+18	−9.7

The difference between the computational values and the values obtained with Eq. (13) is lower than 8%, except in the case with highest peak density and highest roughness, where it is 11% (see Table 6).

In order to check the adequacy of the fitting function to calculate the length correction factor for different channels, five additional models have been built. The main characteristics of these models are summarized in Table 5. The roughness parameters of these models are within the range of those of the first five models, or below the lower limit. In particular, model 10 is based on actual roughness parameters of a real plunger surface measured by means of confocal microscopy (see Fig. 10). Its roughness parameters are within the initially studied range, but its peak density is quite lower (500 peaks/mm^2).

Eq. (13) predicts well the computational results of ξ, including the values of the five additional models that have not been used for the fitting. The deviation of the calculated ξ with respect to ξ_{CFD} is always below 8%, except for one case with 11% (see Table 6). The final deviation of the flow resistance values with respect to the ones obtained with the CFD models is within a $[-10\%, +10\%]$ interval (see Table 6), except for three cases $(11\%, 15\%, 23\%)$, corresponding to cases with very high relative roughness (around 20%) and high peak density (>33,000 peaks/mm^2).

Therefore, it can be concluded that the described length correction function is suitable for correcting the channel length for cases with peak density values in the studied range, from 500 peak/mm^2 up to 120,000 peaks/mm^2, and relative roughness values at least up to 15%. For channels with low roughness values, either the initial method, using the nominal channel length, or the new one, using the effective length, can be used. It is interesting to realise that a relative roughness of 15% means that the channel height represents only three times the average roughness, indicating either a very narrow channel, a very high roughness or a deep penetration of the surfaces that form the channel (the channel is nearly closed).

The methodology herein described could also be used for deriving length correction factors for other types of microchannels, or microchannels with even higher roughness values than those considered in this work.

4. Conclusions

A method for taking into account the effects of very high roughness in the calculation of the fluid flow through microchannels has been presented, based on the introduction of a length correction factor into the calculation method presented in [1]. The correlation of the developed method with CFD results is very good, and shows its validity for channels with relative roughness values up to 15% and peak densities up to 120,000 peaks/mm^2.

References

[1] J.R. Valdés, M.J. Miana, T. Pütz, Numerical investigation of the influence of roughness on the laminar incompressible fluid flow through annular microchannels, Int. J. Heat Mass Transfer 50 (2007) 1865–1878.
[2] S.M. Flockhart, R.S. Dhariwal, Experimental and numerical investigation into the flow characteristics of channels, J. Fluids Eng. 120 (1998) 291–295.
[3] B. Xu, K.T. Ooi, N.T. Wong, W.K. Choi, Experimental investigation of flow friction for liquid flow in microchannels, Int. Commun. Heat Mass Transfer 27 (2000) 1165–1176.
[4] H.H. Bau, J.N. Pfahler, Experimental observations of liquid flow in micro conduits, in: Proceedings of 39th AIAA Aerospace Science Meeting & Exhibit, Reno, NV, 8–11 January 2001, AIAA paper 2001-0722.
[5] J. Judy, D. Maynes, B.W. Webb, Characterization of frictional pressure drop for liquid flows through microchannels, Int. J. Heat Mass Transfer 45 (2002) 3477–3489.
[6] D. Liu, S.V. Garimella, Investigations of liquid flow in microchannels, AIAA J. Thermophys. Heat Transfer 18 (2004) 65–72.
[7] H.Y. Wu, P. Cheng, Friction factors in smooth trapezoidal silicon microchannels with different aspect ratios, Int. J. Heat Transfer 46 (2003) 2519–2525.
[8] M.J. Kohl, S.I. Abdel-Khalik, S.M. Jeter, D.L. Sadowski, An experimental investigation of microchannel flow with internal pressure measurements, Int. J. Heat Mass Transfer 48 (8) (2005) 1518–1533.
[9] K.C. Toh, X.Y. Chen, J.C. Chai, Numerical computation of fluid flow and heat transfer in microchannels, Int. J. Heat Mass Transfer 45 (2002) 5133–5141.
[10] P.S. Lee, S.V. Garimella, D. Liu, Investigation of heat transfer in rectangular microchannels, Int. J. Heat Mass Transfer 48 (9) (2005) 1688–1704.
[11] W. Qu, I. Mudawar, Experimental and numerical study of pressure drop and heat transfer in a single phase microchannel heat sink, Int. J. Heat Mass Transfer 45 (2002) 2549–2565.
[12] J. Yue, G. Chen, Q. Yuan, Pressure drops of single and two-phase flows through T-type microchannel mixers, Chem. Eng. J. 102 (2004) 11–24.
[13] W. Yang, J. Zhang, H. Chen, The study of flow characteristics of curved microchannels, Appl. Therm. Eng. 25 (13) (2005) 1894–1907.
[14] G. Croce, P. D'Agaro, Numerical analysis of roughness effect on microtube heat transfer, Superlattices Microstruct. 35 (2004) 601–616.
[15] F. White, Fluid Mechanics, McGraw-Hill, 1979 (Chapter 6).
[16] Fluent Inc., Fluent Users Guide, Cavendish, Lebanon NH, USA, April 2005.
[17] S.V. Patankar, Numerical Heat Transfer and Fluid Flow, Hemisphere, Washington, DC, 1980.
[18] S.R. Mathur, J.Y. Murthy, A pressure-based method for unstructured meshes, Numer. Heat Transfer 31 (1997) 195–215.
[19] S.E. Kim, S.R. Mathur, J.Y. Murthy, D. Choudhury, A Reynolds-Averaged Navier Stokes Solver Using Unstructured Mesh-Based Finite Volume Scheme, AIAA-Paper 98-0231, 1998.
[20] D.J. Phares, G.T. Smedley, J. Zhou, Laminar flow resistance in short microtubes, Int. J. Heat Fluid Flow 26 (2005) 506–512.
[21] S. Shen, J.L. Xu, J.J. Zhou, Y. Chen, Flow and heat transfer in microchannels with rough wall surface, Energy Convers. Manage. 47 (2006) 1311–1325.
[22] W.L. Qu, G.M. Mala, D.Q. Li, Pressure driven water flows in trapezoidal silicon microchannels, Int. J. Heat Mass Transfer 43 (2000) 353–364.